

Data-driven estimation of the sensitivity of target-oriented time-lapse seismic imaging to source geometry

Andrey H. Shabelansky¹, Alison Malcolm¹, and Michael Fehler¹

ABSTRACT

The goal of time-lapse imaging is to identify and characterize regions in which the earth's material properties have changed between surveys. This requires an effective deployment of sources and receivers to monitor the region where changes are anticipated. Because each source adds to the acquisition cost, we should ensure that only those sources that best image the target are collected and used to form an image of the target region. This study presents a data-driven approach that estimates the sensitivity of target-oriented imaging to source geometry. The approach is based on the propagation of the recorded baseline seismic data backward in time through the entire medium and coupling it with the estimated perturbation in the subsurface. We test this approach using synthetic surface seismic and time-lapse VSP field-data from the SACROC field. These tests show that the use of the baseline seismic data enhances the robustness of the sensitivity estimate to errors, and can be used to select data that best image a target zone, thus increasing the signal-to-noise ratio of the image of the target region and reducing the cost of time-lapse acquisition, processing, and imaging.

INTRODUCTION

Time-lapse seismic imaging is a method used for monitoring and identifying changes within a reservoir. It is often only the changes and not the underlying structure that are of interest. Thus, to obtain a time-lapse image of a reservoir without collecting or imaging a large data set, one needs to know what data collected on the surface (or in wells) contribute most to the reconstructed image of the reservoir region. Typically, an optimal survey design together with an illumination analysis (e.g., Curtis, 1999; van den Berg and Curtis, 2003; Khodja et al., 2010) is performed to optimize seismic acquisition

before the actual data collection. Ray-based methods are conventionally used for illumination analysis (Bear et al., 2000). However, the approximations in ray theory severely limit the accuracy of the analysis in complex regions (Hoffmann, 2001). Wave-equation-based methods are used to alleviate the limitations of ray-based approaches (Xie et al., 2006; Xie and Yang, 2008). Even with these methods, it remains difficult to obtain reliable time-lapse acquisition geometries because these methods do not include the sensitivity of the target regions to time-lapse acquisition geometries. Denli and Huang (2010) present an approach that establishes a sensitivity relationship between the changes in geophysical model parameters and the receiver geometry on the surface. Their approach, as well as the approaches mentioned above, still use only model information and are based on forward-modeling a considerable number of shots (or rays) covering an entire seismic acquisition.

Our approach is similar to that described in Denli and Huang (2010); however, instead of forward propagating a point source, as in Denli and Huang (2010), we use a data-driven approach in which the recorded baseline seismic data are propagated backward in time. The sensitivity relationship is estimated from the scattered sensitivity wavefield, which is calculated using a first-order perturbation of the wave equation with respect to wave velocity or density. The scattered radiation pattern from the presumed perturbations can be predicted by the method described in, e.g., Aki and Richards (1980) (pages 728–737), Wu (1989), and is a function of the characteristic scale of the perturbation (e.g., diameter in the case of a circular perturbation in 2D), mean frequency of the data, and the perturbation type (wave velocity or density). The data-driven formulation makes the sensitivity analysis sensitive not only to the presumed changes in the geophysical structure, but most importantly dependent on the properties of the baseline data. The estimated sensitivity relationship indicates which shot records are most important in a subsequent time-lapse acquisition, which can reduce the costs of the time-lapse acquisition for target-oriented imaging. By using the baseline data as an integral part of the calculation, we show that we improve the robustness of the method to errors in the velocity

Manuscript received by the Editor 10 May 2012; revised manuscript received 3 October 2012; published online 1 March 2013.

¹Massachusetts Institute of Technology, Earth Resources Laboratory, Cambridge, Massachusetts, USA. E-mail: andreys@mit.edu; amalcolm@mit.edu; fehler@mit.edu.

© 2013 Society of Exploration Geophysicists. All rights reserved.

model and the estimated perturbation. We refer to the proposed algorithm as reverse-time wave sensitivity (RTWS).

In this paper, we outline the underlying theory for our method and test it with three examples: two synthetic models and one field data set. The first example is a simple single-reflector model that illustrates the directionality of the sensitivity field of a single surface source and its relationship with the geometry of the perturbed region. The second example is the Marmousi model (Versteeg and Grau, 1991) with which we examine the stability of RTWS to different inputs, and show the merit of RTWS method over the forward approach, described in Denli and Huang (2010). The third example is a walkaway VSP time-lapse data set where we show that shots chosen based on RTWS image the region of interest with increased signal-to-noise ratio (S/N), as compared to an image formed with all shots. Although not addressed here, RTWS could be used in the same manner for target-oriented full-waveform inversion.

REVERSE TIME WAVE SENSITIVITY

To establish the relationship between the seismic data recorded on the surface and the region of interest inside the earth, we use the principle of time-reversibility stating that, when a recorded shot gather is numerically back propagated in time with the correct velocity and density models, its energy will fully collapse into a single point at the initial position of the source. If the medium (velocity and density models) is perturbed for the back-propagation, then the back-propagated wavefield will no longer focus perfectly at its initial source position and instead some energy will arrive at other positions. To isolate the back-propagated energy due only to the perturbation, we design an algorithm in which the wavefield generated by the perturbation is separated from the total wavefield at each time step of the back-propagation. The detailed mathematical derivation is given in Appendix A.

This algorithm, RTWS, consists of two steps (Figure 1), where each step uses full-wave equation propagation. The first step is the propagation of the seismic shot record backward in time down to the region of interest as in reverse-time migration (RTM) (Baysal et al., 1983). We refer to this as the illuminating back-propagated wavefield. The second step is the generation of a second wavefield, referred to as the scattered-sensitivity wavefield, which is back-propagated in time back to the surface. This wavefield is calculated from the coupling between the illuminating back-propagated wavefield and the perturbation in either wave velocity or density. Although the method can be derived for any type of wave equation (acoustic, elastic, viscoelastic), for the sake of simplicity, we use an acoustic 2D derivation resulting in the following set of equations

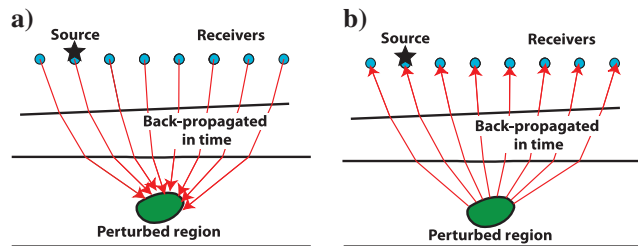


Figure 1. Two steps of RTWS: (a) Propagating the recorded seismic data backward in time from the receiver locations toward the perturbed region, (b) Propagation of the scattered-sensitivity wavefield backward in time from the perturbed region toward the surface.

$$\frac{\partial^2}{\partial t^2} \begin{pmatrix} P_i \\ S_i \end{pmatrix} = \begin{pmatrix} c_b^2 \rho_b \nabla \cdot \frac{1}{\rho_b} \nabla & 0 \\ -c_p^2 V & c_p^2 \rho_2 \nabla \cdot \frac{1}{\rho_p} \nabla \end{pmatrix} \begin{pmatrix} P_i \\ S_i \end{pmatrix} - \begin{pmatrix} f_i \\ 0 \end{pmatrix}, \quad (1)$$

where time t is propagated backward from the maximum recorded time T toward the start of recording ($t = 0$). The operator ∇ and $\mathbf{x} = (x, z)$ are the spatial gradient and spatial coordinate consisting of position x and depth z . We denote by $c(\mathbf{x})$ and $\rho(\mathbf{x})$ the velocity and density and by subscripts b and p the background and perturbed models, respectively. We will also refer to the background and perturbed models as baseline and monitor models, respectively. For the source index i , $P_i(\mathbf{x}, t)$, $S_i(\mathbf{x}, t)$, and $f_i(x, t)$ are, the illuminating field (assumed to be pressure), the scattered-sensitivity field, and the data (i.e., a shot record), respectively. Note that the scattered-sensitivity wavefield satisfies a standard wave equation with a source from the perturbations. The perturbation operator $V(\mathbf{x}, t)$, derived in Appendix A, is given as

$$V(\mathbf{x}, t) = \rho_p \nabla \cdot \frac{\delta \rho}{\rho_b^2} \nabla - \delta \rho \nabla \cdot \frac{1}{\rho_p} \nabla - \frac{2\delta c}{c_b^3} \frac{\partial^2}{\partial t^2}, \quad (2)$$

where the perturbations are defined as

$$\delta c = c_p - c_b \quad \delta \rho = \rho_p - \rho_b.$$

Note also that the perturbations (δc , $\delta \rho$) in the perturbation operator act not only as a source for the scattered-sensitivity field, but also affect the radiation pattern of the scattered wavefield through the geometric shape of the perturbation. Because this derivation is based implicitly on the Born approximation, we need to satisfy the following condition (e.g., Wu, 1989)

$$\frac{\delta \nu a}{\nu_b \lambda} \ll 1, \quad (3)$$

where λ is the wavelength of the (illuminating) wavefield, ν is velocity or density, and a is the size of the geometrical perturbation (e.g., diameter in the case of spherical perturbation).

Because the sensitivity-scattered wavefield S_i is the wavefield generated from the perturbed region, its high energy as a function of \mathbf{x} indicates good illumination of the perturbed region by a source (or by reciprocity a receiver) at the location \mathbf{x} , and conversely for low energy. We estimate this sensitivity energy via

$$E_i(\mathbf{x}) = \int_T^0 S_i^2(\mathbf{x}, t) dt. \quad (4)$$

Although we generally estimate the sensitivity either at the surface ($z = 0$) or in a well ($x = x_0$), we can extract it at any point (\mathbf{x}) giving us the sensitivity of a source at \mathbf{x} to the perturbation.

Thus far we have described the method for a single shot. To estimate the sensitivity of an entire survey and to illuminate the perturbation from different possible directions, we sum the energy given above over shots to calculate the final energy E as

$$E(\mathbf{x}) = \sum_{i=1}^{N_s} E_i(\mathbf{x}), \quad (5)$$

where N_s is the number of shots used to calculate the sensitivity. We then need to address the question of how many and which shots to include in the summation to obtain a reliable and stable final energy profile. We address this with numerical examples in the following sections.

TESTS ON SYNTHETIC DATA

We first test the proposed algorithm with two synthetic models. The first synthetic is a single-reflector model which allows us to illustrate the details of the RTWS algorithm and show how it uses the advantages of back-propagation. The second model is the Marmousi model with which we demonstrate the stability and robustness of the RTWS method, and show the merit of the RTWS over the forward sensitivity approach of Denli and Huang (2010). All synthetic data and the sensitivity wavefield in equation 1 are modeled with a 2D finite-difference solver, using a second order in time staggered-grid pseudospectral method with perfectly matched layer (PML) absorbing boundary conditions (Kosloff and Baysal, 1982; Carcione, 1999; Marcinkovich and Olsen, 2003).

Single-reflector synthetic model

With this test, we illustrate how the geometry of the perturbed region and the type of perturbation (velocity or density) affect the directionality of the backward sensitivity wavefield. To this end, we create baseline velocity and density models of a single flat reflector at the depth of 1 km, through which we generate a shot gather for a source located at $x = 0.36$ km on the surface. The velocity and density values are 2300 m/s and 2300 kg/m³ above the reflector, and 2500 m/s and 2500 kg/m³ below the reflector, respectively. The number of grid points N_x and N_z are 120, and the grid sizes Δx and Δz are 12 m. The receivers are equally distributed on the surface and span the same grid as the sources. We use a Ricker wavelet with a peak frequency of 50 Hz and a time step of 1 ms. Figure 2 shows a snapshot at 1 s of the back-propagated in time illuminating wavefield, P_i . From this wavefield, we compute the RTWS for four perturbations: two for a point perturbation in velocity and density and two for an extended circular perturbation in velocity and density. All perturbations are centered at $(x, z) = (0.72, 0.72)$ km, and

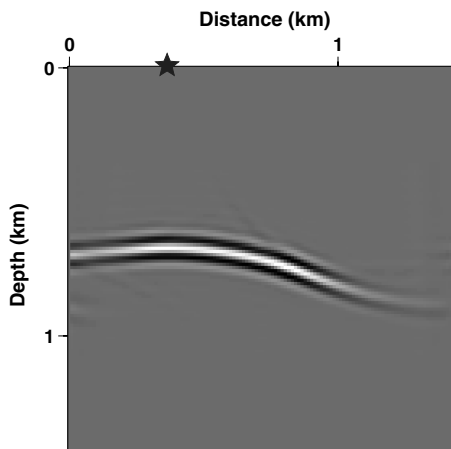


Figure 2. The snapshot of the back-propagated illuminating wavefield at $t = 1$ s. The star on the surface indicates the source location at 0.36 km.

the diameter of the circular perturbation is 144 m (12 grid points), which is larger than the smallest wavelength contained in the data, $\lambda = 23$ m. In both cases, the perturbation ($\delta\nu = \nu_p - \nu_b$) is negative and equals 5% of the baseline value. Figure 3 shows snapshots of the reverse sensitivity S_i wavefield at time 1 s, where the back-propagated wavefield P_i is coupled with each of the two perturbations in the velocity and density models.

In Figure 3a, we observe that, for a single point velocity perturbation, the backward-propagated sensitivity wavefront S_i is isotropic. However, for the circular perturbation we observe that the sensitivity wavefront is no longer isotropic but is stronger in the forward scattering direction (Figure 3b). This orientation of the sensitivity wavefield is controlled, not only by the fact that the diameter of the perturbation is larger than the minimum wavelength of the propagation, but also by the position of source i , here at 0.36 km on the surface. The back-propagation of this shot record defines the directions of the illumination P_i as well as that of the formed sensitivity S_i . Note that the reflector is placed (at 1 km) below the perturbation to ensure that the generated scattered-sensitivity wavefield will be reflected from the reflector and recorded at the receivers on the surface. In Figure 3c and 3d, we perform the same tests with perturbations in density. For a single point density perturbation, we observe that the scattering sensitivity wavefield is no longer isotropic (see Figure 3c), and its energy is predominantly in the back-scattered direction. We observe the same back-scattering behavior for the circular density perturbation (Figure 3d); however, it is more complicated than the single point perturbation because of the wave interference generated from the edges of the perturbation.

In Figure 4, we show the sensitivity energy profiles from velocity and density perturbations, calculated using equation 4, for the

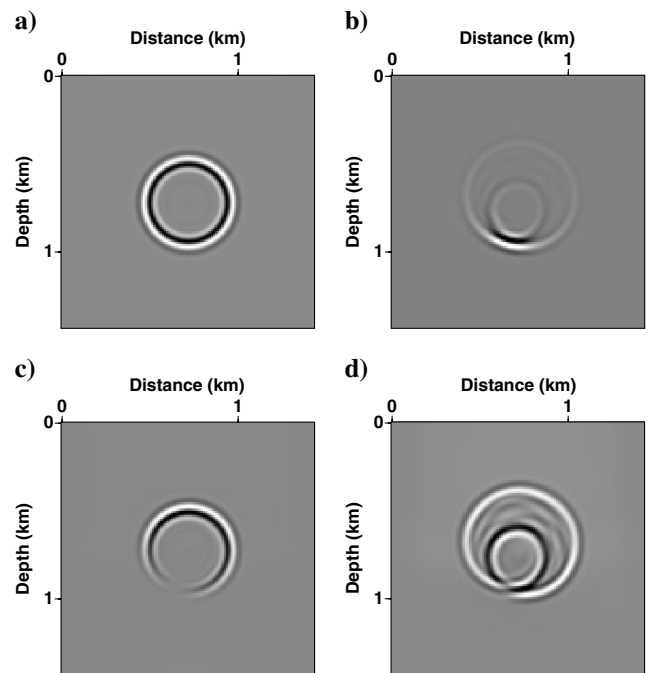


Figure 3. The snapshots of the reverse-time scattered-sensitivity wavefront at $t = 1$ s, generated with the input shot at 0.36 km and (a) single point velocity perturbation, (b) circular velocity perturbation, (c) single point density perturbation, and (d) circular density perturbation. Note the strong directionality of the sensitivity wavefront for the extended velocity perturbation in (b).

sensitivity wavefields at the surface. High sensitivity energy at point x indicates that the region of the perturbation is well illuminated by a source at x , and conversely for low-sensitivity energy. Note that the sensitivity energy profiles are always shown normalized between zero and one because it is the positions of the high-energy peaks rather than their absolute value that is important.

In the energy profiles (Figure 4), we observe the increased importance of the forward- and back-scattering; the peak energy observed for the velocity perturbation (Figure 4b) is accumulated on the opposite side of the scatterer from what is observed for the density perturbations (Figure 4c and 4d), although the resolution of these energy profiles is fairly poor in comparison with those generated from an extended velocity perturbation (Figure 4b). These observations, along with those made with Figure 3, and along with the predictions given in Aki and Richards (1980) (pages 728–737), lead us to conclude that because a contrast in density results in a primarily back-scattered field, applying RTWS assuming such a contrast gives valuable complementary information about the illumination of the target (assuming the target region contains velocity and density contrasts) to that caused by the forward-scattering from a velocity contrast.

The sensitivity energy profiles shown in Figure 4 are generated for a single shot gather. To establish a complete relationship between the perturbed region and the sensitive source locations, we need to incorporate the calculated sensitivity energy for several shot gathers into a final profile. In the next section, we show that it is sufficient to calculate the sensitivity energy for a relatively small number of shot gathers.

Marmousi model

To test the algorithm on a more realistic model, and to illustrate the importance of the baseline model for sensitivity analysis, we use the Marmousi synthetic model (Versteeg and Grau, 1991) with $N_x = 287$ and $N_z = 150$, through which we generate 123 shot re-

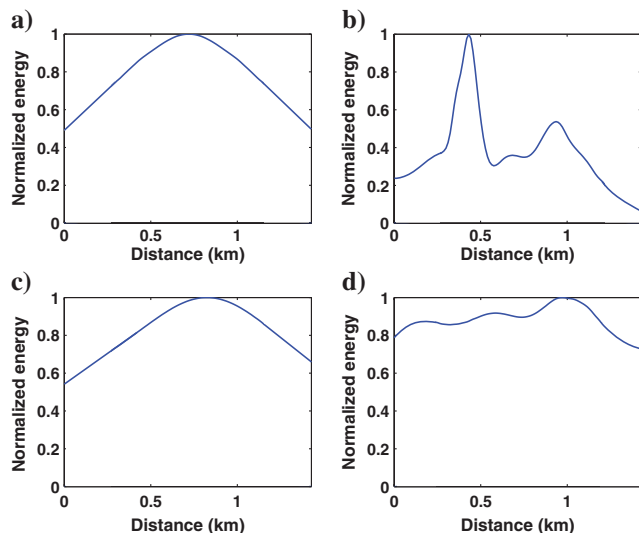


Figure 4. Reverse sensitivity energy profiles recorded on the surface to illustrate which shots are expected to be most sensitive to the perturbed region in the velocity model for (a) point diffractor, (b) circular perturbation, and in the density model for (c) point diffractor, (d) circular perturbation.

cords with an interval of 24 m using a Ricker wavelet with peak frequency of 30 Hz. The receivers are equally distributed on the surface with interval of 12 m, and span the same grid as the sources. The grid sizes Δx and Δz are 12 m. The density is constant throughout the model.

Sensitivity analysis due to a point-velocity perturbation

To construct a perturbed model, we add a single point perturbation at $(x, z) = (1.92, 0.948)$ km (marked with an arrow in Figure 5). Next, we calculate the reverse sensitivity for three surface seismic shot records with sources located at 1.5, 2.1, and 2.7 km. The result is shown in Figure 6. In this figure, we observe that we obtain a very similar sensitivity energy profile for each source position. This is because a point perturbation in velocity results in an omnidirectional scattered sensitivity field as shown in Figure 3a. This suggests that, for this example, a reliable estimate of the source sensitivity with respect to a point perturbation in velocity can be obtained with a single (or very few) shot.

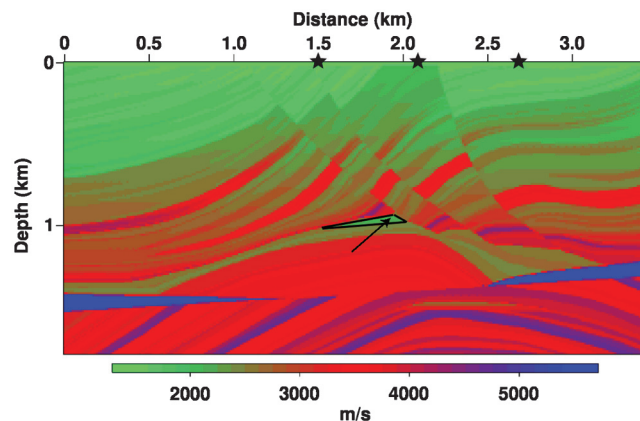


Figure 5. Marmousi velocity model with two perturbations: a single point perturbation at $(x, z) = (1.92, 0.948)$ km (marked by the arrow), and an extended triangular perturbation (marked by the black triangle). The sensitivity analysis for each perturbation is performed independently. The stars on the surface indicate the source locations.

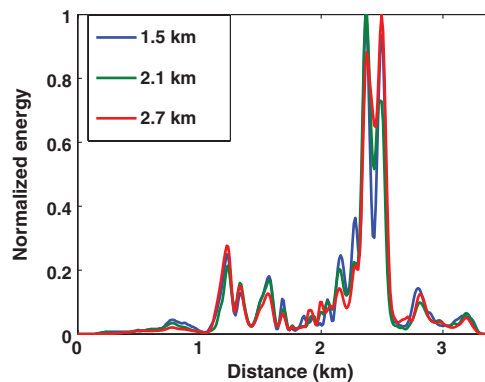


Figure 6. The reverse-time sensitivity energy profile recorded on the surface illustrates the relationship of each source position with a point perturbation in the velocity model. The similarity of the profiles computed for different shot locations indicates that the total energy can be estimated based on relatively few shots.

To show the applicability of the RTWS algorithm to imaging, we construct target-oriented images using sources chosen based on the reverse sensitivity energy profile. Here, the imaging of the perturbation itself is not the main interest of our algorithm because in practice the exact time-lapse perturbation is hard to predict. Instead, we are interested in imaging the vicinity of this perturbation. By choosing four shot gathers, modeled with the monitor velocity model, with the highest sensitivity energy in Figure 6 (at positions 1.24, 2.39, 2.51, and 2.83 km), we form an image (Figure 7a) using the RTM algorithm (Baysal et al., 1983) with Laplacian filter (Youn and Zhou, 2001). For comparison, we form three additional images (Figure 7b, 7c, and 7d). Figure 7b is migrated with four shot gathers that correspond to lowest sensitivity energy (at positions 1.44, 1.75, 1.97, and 2.66 km), and Figure 7c is migrated with shots, chosen arbitrarily (at positions 1.38, 1.8, 2.22, and 2.64 km). Figure 7d is shown as a reference image formed using all 123 shots (with shot spacing of 0.024 km). These results show that the image made with the four shots located at the positions having the highest sensitivity energy has better illumination of the vicinity of the perturbation, denoted by the arrow, than those made with the arbitrary or the lowest energy; this image is of similar quality to that made with all 123 shots.

Sensitivity analysis due to an extended (triangular) velocity perturbation

In the previous sections, we found that a point perturbation in velocity does not produce a directionally dependent scattered-sensitivity wavefield. To investigate the influence of perturbation shape in the Marmousi model, we add a larger triangular perturbation

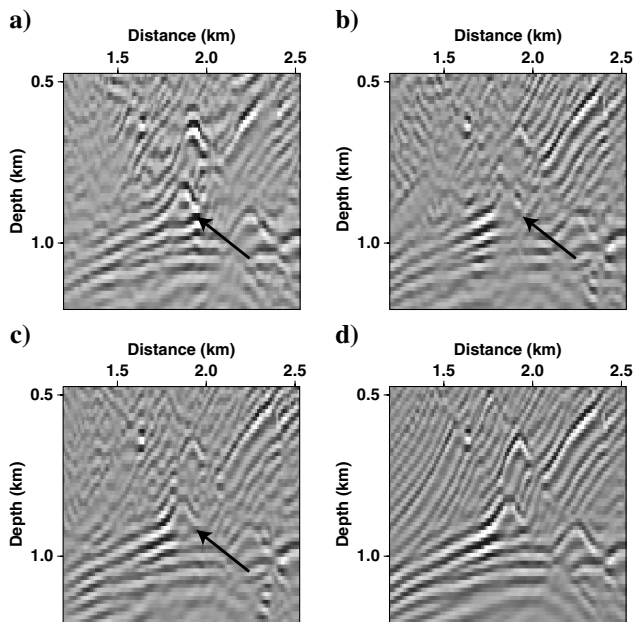


Figure 7. RTM images migrated with four shots, chosen based on: (a) maximum reverse sensitivity energy (positions 1.24, 2.39, 2.51, and 2.83 km), and (b) minimum reverse sensitivity energy (positions 1.44, 1.75, 1.97, and 2.66 km), both generated from a single point perturbation in velocity model at $(x, z) = (1.92, 0.948)$ km. (c) RTM image with four arbitrary equally spaced shots located at positions (1.38, 1.8, 2.22, and 2.64 km). (d) RTM image migrated for reference with all 123 shots with equally spaced increment of 0.024 km.

(marked by a black triangle in Figure 5), whose height and width are 160 and 540 m (approximately three and ten minimum wavelengths), respectively. We calculate the sensitivity energy profiles with the same shot records as we used with the single point perturbation; these profiles are shown in Figure 8.

In this figure, we observe that the energy profiles for each source location are different. Therefore, we need to estimate the sensitivity for each surface seismic record and incorporate its energy into the final energy profile. In this test, however, by summing the sensitivity energies from a sparse distribution of sources fully covering the expected range of source locations, we observe that a reliable estimate of the total sensitivity is obtained by summing over only a few sources (see Figure 9a). Note that the peaks in the profiles converge to the same locations after a relatively small number of sources are used: the maximum difference in peak location is only 0.072 km when summing five of the 123 profiles compared to using all 123 shots. To test this observation, we compute the difference in sensitivity energy (equation 5) between the summation obtained when using the total number of shots ($N_s = 123$) and that obtained for a given number of shots spanning the acquisition. In other words, we compute

$$\epsilon_k = \sum_{n=1}^{N_x} \left| \sum_{i=1}^{N_s} E_i(x_n, z_0) - \sum_{i=1}^k E_i(x_n, z_0) \right|, \quad (6)$$

where N_x is the number of computational grid points at the surface. Note that this formula assumes small perturbations in the locations of the peaks, and thus might need to be modified for the large perturbations.

Figure 9b shows the normalized ϵ as a function of the number of shots k used in the calculation. We observe that we need only a limited number of shots to establish a reliable sensitivity using RTWS. Therefore, by choosing the four source positions with the highest sensitivity energy from the summed profile over five shots in Figure 9a (at 0.96, 1.296, 1.632, and 2.352 km), we form a target-oriented image. This image of the perturbed region (marked by the triangle in Figure 5) is shown in Figure 10a. For comparison, we form three additional images, shown in Figure 10b, 10c, and 10d. The image shown in Figure 10b is obtained by migrating four shot gathers that correspond to the lowest sensitivity energy (at positions 1.152, 1.488, 2.016, and 2.688 km); Figure 10c is obtained using

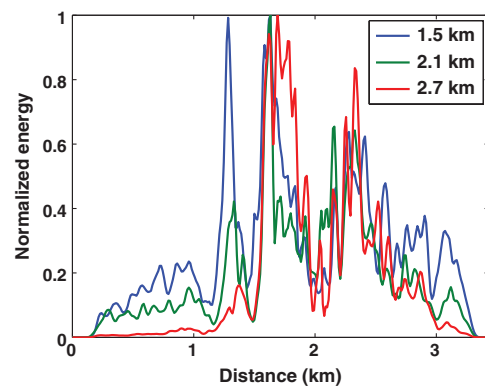


Figure 8. Reverse sensitivity energy profiles generated by the triangular velocity perturbation from shots at positions: 1.5, 2.1, and 2.7 km.

four equally spaced shots (at positions 1.44, 1.68, 1.92, and 2.16 km). Figure 10d shows a reference image made using all 123 shots (with equal spacing of 0.024 km). The image made with the four high-sensitivity shots images the perturbed region, marked by an arrow, better than either the low-sensitivity or uniformly spaced shots and in fact, as in the previous example, makes an image that is of similar quality to that obtained when using all 123 shots.

Merit of RTWS over a forward sensitivity approach

Thus far, we have demonstrated the properties of the RTWS method and illustrated how it can be used to estimate the locations

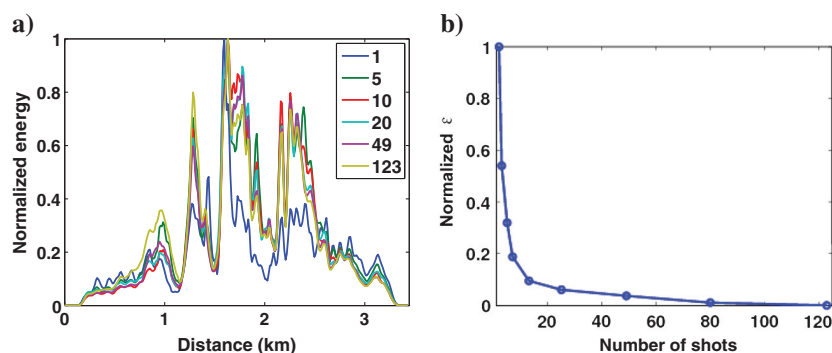


Figure 9. (a) A comparison of energy profiles obtained by using progressively more source locations. Note that the locations of the peaks become stable quickly and entire profile is stable well before all 123 shots are included. (b) Normalized differential energy computed with equation 6, using equally distributed shots.

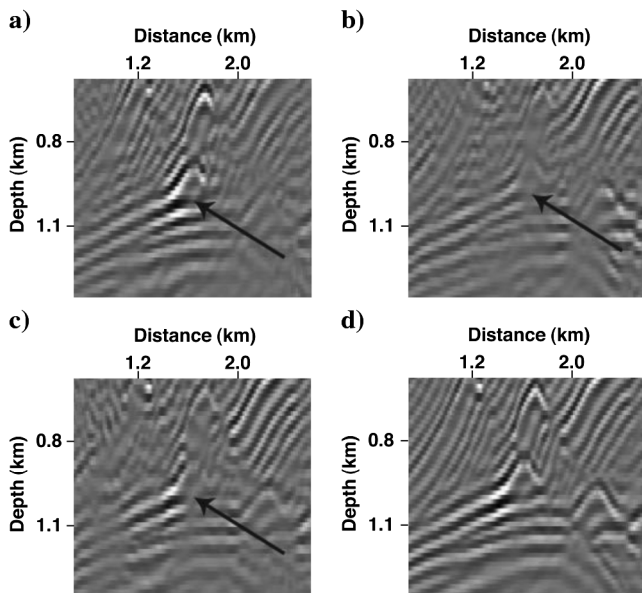


Figure 10. RTM images from migrating four shots using: (a) maximum reverse sensitivity energy (positions 0.96, 1.296, 1.632, and 2.352 km), and (b) minimum reverse sensitivity energy (positions 1.152, 1.488, 2.016, and 2.688 km), both generated from the triangular perturbation shown in Figure 5. (c) RTM image with four arbitrary equally spaced shots (located at positions 1.44, 1.68, 1.92, and 2.16 km). (d) A reference RTM image with all 123 shots with equally spaced increment of 0.024 km. The black arrows on the images refer the perturbed region.

that are most sensitive to a perturbed region. In this section, we compare RTWS to a similar forward source sensitivity approach, as given in Denli and Huang (2010). To perform a valid comparison, still using the Marmousi model, we calculate forward sensitivity energy profiles for all 123 shots, sum all of them into a final profile, and compare the final profile with that produced by RTWS (the profile in Figure 9a that was obtained from the summation over 123 shots). The forward approach estimates the sensitivity of a specific region in the earth to receiver geometry, and the reverse approach, RTWS, estimates the sensitivity of the same region to source geometry. Therefore, the use of all shots and all receivers on the same grid yields the same sensitivity relationship between specific perturbation in the earth and the source-receiver geometry.

Figure 11a shows the comparison. For the forward approach, we use the same finite-difference algorithm as used for RTWS; however, instead of propagating the seismic shot records backward in time, we propagate a point source forward to time T , the maximum recorded time in the shot gathers. Note that the input seismic data for RTWS was calculated using the same velocity model as is used as the background velocity for the sensitivity estimation.

We observe in Figure 11a that the forward and reverse sensitivity energies are similar in the center, between 1 and 2.2 km. At the edges, however, we observe that the reverse sensitivity energy is more attenuated than the forward energy, even though the peaks of the energy are at the same locations. This is explained by the fact that the forward illuminating wavefield

can hit the perturbed region and generate the sensitivity wavefield, which is then recorded at the receivers on the surface, whereas the illuminating wavefield (in the baseline model) may not be recorded by the receivers and so will not be part of the (in this case modeled pressure) data that are back-propagated in RTWS. This edge effect is less severe when less complicated models and more receivers are used.

Having established that the two approaches give similar results away from the boundary of the model for the exact velocity, we now investigate the robustness of both methods to errors in the background velocity models. To model this, we smooth the background (Marmousi) model and add the same triangular perturbation to the monitor model. Smoothing is done using a median filter with a window size of 85 m (about 2λ where λ is the minimum wavelength). For RTWS, we use seismic data computed using the original, unsmoothed model but back-propagate in the smoothed model.

In Figure 11b and 11c, we show the comparison between the summed 123-shot sensitivity profiles generated by reverse sensitivity approach, RTWS, and that by the forward approach, with the original and the smooth baseline velocity models. Despite the loss of the sharpness of the energy obtained by the RTWS (Figure 11b), we observe that the energy distribution is still preserved (see high-energy peaks at e.g., 1.296, 1.632, and 2.352 km), whereas for the forward sensitivity approach, given in Figure 11c, peaks defining the high-energy source locations have disappeared. This indicates that we can not expect to form a good image with the shots chosen based on the forward sensitivity profiles in the presence of velocity uncertainty. This observation suggests that the use of the recorded

seismic data improves the robustness of the sensitivity estimates when the background models are not well known.

The stability of RTWS

In this section, we continue our analysis of the stability of the RTWS method using three numerical examples with the Marmousi model. Because we observed above that the energy profile summed over five shots reliably represents the sensitivity of source locations (Figure 9a), we use the energy profiles from these same five shot locations in all of the examples in this section. The examples chosen below test the stability of the RTWS to various potential uncertainties in an estimated perturbation, its geometrical shape, and the scale of the perturbation relative to the frequency content of the seismic data. In the last example, we show the comparison of the RTWS estimates between profiles produced with acoustic and elastic input (baseline) data. Note that these examples are not meant to provide an exhaustive set of the stability tests, but instead to show that the method is robust to some errors and inaccuracies.

Stability with respect to the velocity perturbation

Having established that RTWS is robust when smoothing the velocity model, we now assess its robustness to errors in the estimated perturbation. To do this, we test RTWS using the same monitor velocity model with the triangular perturbation as in Figure 5 (marked by the black triangle) with an additional 50% uniformly distributed random noise within the perturbed region to simulate errors in our a priori estimate of the perturbation. Figure 12a illustrates the comparison for the same summed five-shot sensitivity profiles generated due to the constant triangular perturbation and that supplemented with the noise. We observe that, although the energy in the profile is decreased to some extent, the peaks in the profiles are preserved despite the high level of added noise.

Stability with respect to the geometric shape of the perturbation

Because the perturbation shape is generally known only approximately, we test the method using an elliptical estimated perturbation for the RTWS instead of the triangular perturbation shown in Figure 5. The major and minor diameters of the elliptical perturbation are of the same size as the width and the height of the triangle, respectively. In Figure 12b, we show the sensitivity comparison between these two perturbations obtained again from the five shots. We observe that most of the peaks in the sensitivity profile are preserved, though with different relative energies. It is interesting to note that the sensitivity profile generated with the elliptical velocity perturbation is similar to that generated from single point perturbation, shown in Figure 6. This observation suggests that, in the presence of a complicated model, the preferred directionality of the scattered-sensitivity wavefield is reduced

and the scale of the perturbation is equally diminished, although the physical scale of the perturbation placed into the model is above the minimum wavelength of the data.

Stability with respect to the frequency content of the (baseline) data

As we showed in the previous sections, the shape of the perturbation is one of the key factors influencing RTWS. The influence of this shape is dependent on the source frequency of the data (inversely proportional to wavelength λ); this means that the sensitivity wavefield generated from a circular-shape perturbation with high frequency data ($a \gg \lambda$) is expected to be similar to that generated by a point scatterer with a low frequency ($a \ll \lambda$). To test how the frequency content of the data affects the estimated sensitivity, we generate five shot gathers at the same positions as used in the previous examples, through the original Marmousi velocity model, but using a source with a lower peak frequency of 20 Hz (the original data were generated with a peak frequency of 30 Hz). We used the original Marmousi velocity model as the baseline model and velocity with the triangular perturbation in Figure 5 as the monitor model. Figure 12c shows the comparison between the five-shot sensitivity profiles with different frequencies; we observe that for lower frequency content, the peaks appear smoother, however the general energy distribution is preserved.

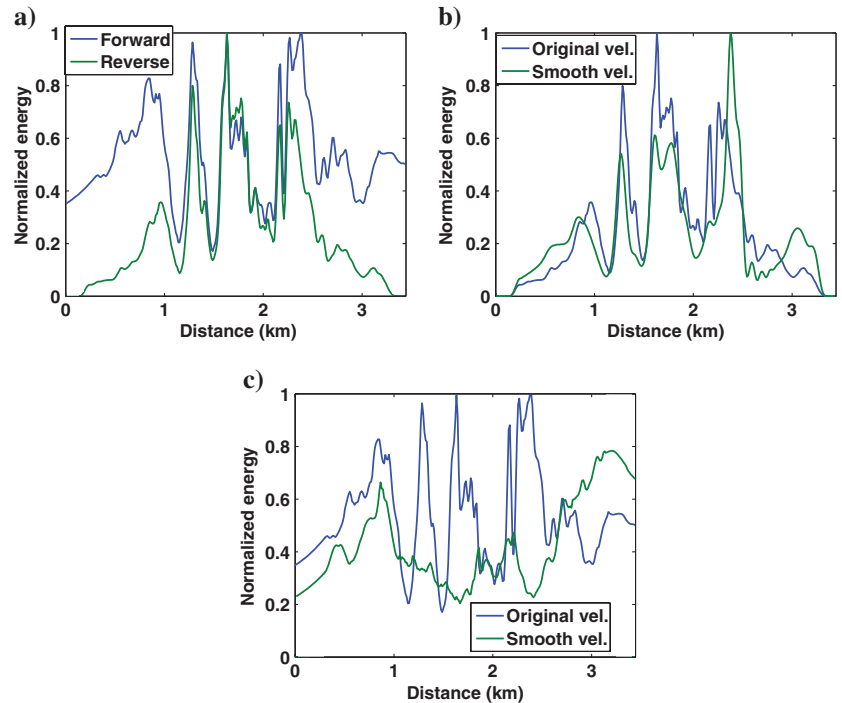


Figure 11. The comparison of the sensitivity energy profiles estimated on the surface with 123-shots between: (a) the forward and the reverse (RTWS) approaches using the correct background velocity (Marmousi), (b) the correct (original) and the smoothed (perturbed) background (Marmousi) velocity models using the reverse (RTWS) approach, and (c) the correct (original) and the smoothed (incorrect) background Marmousi velocity models using the forward approach presented in Denli and Huang (2010). The perturbed (monitor) model was generated by the same triangular inclusion into the background models.

Stability with respect to the input data: Acoustic and elastic

Because seismic data are not acoustic, we compare the estimates of the RTWS method produced with acoustic and elastic input (baseline) seismic data. The elastic data are generated with a constant V_P/V_S ratio of 2 and the same parameters as the acoustic data, whose parameters are listed above. Figure 12d shows the comparison where we observe that the sensitivity energy from acoustic and elastic input data is qualitatively similar (preserving the high-energy peaks), although the effect of the converted wave energy is observed as well, especially at the edges. Nevertheless, when the model is less complicated, we expect the effect of the converted waves to be less severe.

DATA SET FROM THE SACROC OIL FIELD

To examine the robustness and applicability of RTWS to a real data set, we choose a time-lapse walkaway VSP from the Scurry Area Canyon Reef Operators (SACROC) enhanced oil recovery (EOR) field, in which a CO₂ sequestration project was monitored. We present this data solely to test the RTWS method with field data, and the interpretation of the time-lapse anomaly will be discussed elsewhere. The data consist of two surveys. The baseline survey was collected before two injections of CO₂ into the reservoir, and the second, monitor, survey was acquired after the injections were completed. Note that, even though the RTWS method does not use the monitor data for estimating the sensitivity of the source locations, we use this data set to form images of the region associated with the perturbation. Each data set contains 97 shots on the surface, sepa-

rated by 36 m, which are recorded at 13 receivers located in the monitor well at depths between 1554.5 and 1737.4 m, with an interval of 15.24 m (Figure 13). The data have a maximum frequency of 100 Hz. Using the reciprocity principle, we interchange the sources and receivers and call this the reciprocal data set. A median filter was applied to the data to remove the downgoing waves (Cheng et al., 2010). The injection wells are located about 200 m to the right of the monitoring well. Because two CO₂ injections were performed at approximate depths of 1.98 and 2.04 km (Wang et al., 2011), we can identify the potential reservoir region where we will place a perturbation. The velocity and density models were acquired from the monitoring well logs, which were vertically smoothed, horizontally extrapolated, and a double difference full wave form inversion (Yang et al., 2011) was applied to adjust the velocity model. Using these velocity and density models, we image the baseline and monitor reciprocal data sets using RTM. The resulting images are shown in Figure 14 along with their difference. The difference is similar to that shown by Wang et al. (2011). The zero value on the horizontal axis refers to the position of the monitor well, in which the receivers were located. As can be seen in the difference image (Figure 14c), the reservoir region (marked with an arrow) is poorly imaged when stacking all of the data as much of the data do not contribute to the imaging of the reservoir region. Therefore, by using RTWS, we attempt to estimate the most sensitive sources on the surface that would image best the region of interest. Using only these sources, we hope to improve the S/N of the image by removing sources that contribute only noise.

We use the reciprocal and not the original data for two reasons.

First, to reduce the number of shot gathers to be back-propagated from 97 to 13, and second because the VSP geometry had a narrow downhole receiver aperture (182.9 m). The latter reason makes the measurements of the scattered-sensitivity energy along the receiver array poorly resolved. Therefore, we calculate the scattered-sensitivity energy on the surface instead of along the original downhole receiver array. Note that the scattered-sensitivity energy defined by equation 4 can be estimated at any spatial grid point. In this example, because the recording time is long enough, the scattered-sensitivity energy can be recorded on the surface. From this wavefield, we then estimate which actual original sources are most important for imaging the target region.

Because we do not possess any well log information collected after the injections, we introduce simple weak perturbations satisfying the condition given by equation 3. The perturbations are of elliptical shape of -1 m/s and -1 kg/m³ and 50% random noise in the velocity and density models, respectively. The horizontal (major) and vertical (minor) diameters of the perturbations are 116 and 95 m (3 and 2.5 minimum wavelengths), respectively, entered 200 m to the right of the monitoring well at a depth of 2.01 km. Note that the perturbation is placed at the location of the injection into the reservoir which is poorly imaged by baseline and monitor data sets (see the region marked with the arrow in

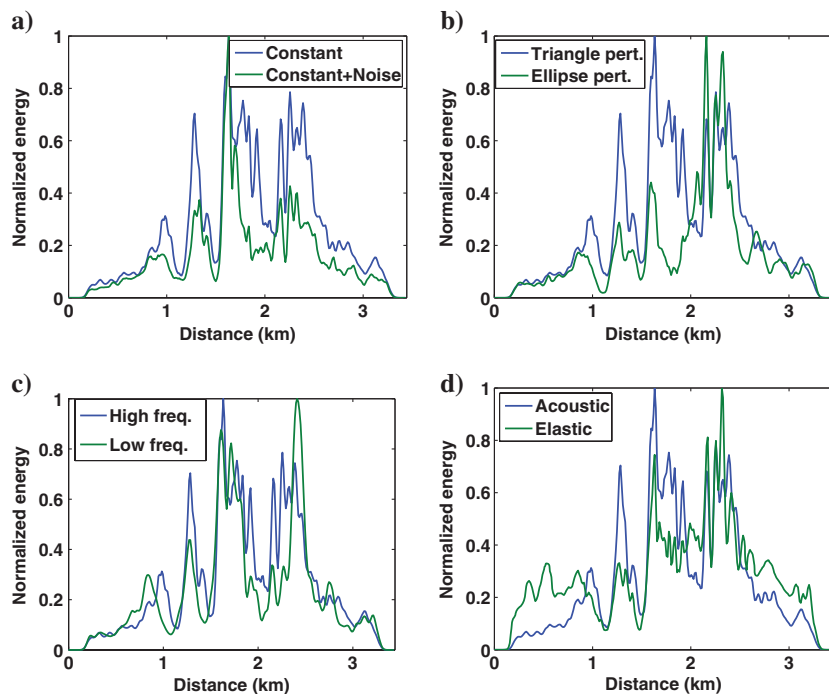


Figure 12. The comparison between the summed five-shot reverse sensitivity energy profiles generated with acoustic data and with the constant triangular perturbation in Marmousi model (Figure 5) and (a) that supplemented with 50% random noise in the perturbed region, (b) that with elliptical shape perturbation, (c) the same baseline and monitor velocity model as described in Figure 5 with triangular perturbation but with different (peak) frequency content: 30 Hz (high) versus 20 Hz (low), and (d) the elastic input data.

Figure 14c), even though we still observe an anomaly at the depth of the CO₂ injection (marked by a circle in Figure 14c).

Using the velocity, density, and baseline seismic shot data we estimate separately the sensitivity energy profiles of RTWS with respect to velocity and density perturbations (see Figure 15). Although these final profiles were obtained by the summation over all 13 reciprocal shot profiles, we observed from the stability of RTWS given by equation 6 that a reliable final energy profile was obtained with the first three shot gathers. This observation is explained again by the vertical geometry of the receivers which has a minor effect on the estimated sensitivity of the sources that are horizontally distributed on the surface. In other words, each (reciprocal) shot gather back-propagated from the surface down toward the (reciprocal) receivers illuminates the reservoir from almost the same directions, and therefore each consecutive back-propagated shot does not add much information. We also observe in Figure 15 that

most of the sensitivity energy due to a velocity perturbation is concentrated around a single peak at -0.015 km. When we choose six (original) shot gathers taken in the vicinity of this maximum peak (at positions -0.195 , -0.158 , -0.122 , -0.085 , -0.049 , and -0.012 km) on the surface, and construct baseline and monitor images together with their difference, shown in Figure 16a, 16b, and 16c, we observe that the amplitudes in the images are smeared between the monitoring and the injection wells. These results are explained by the strong preferred-orientation property of the scattered-sensitivity wavefield generated from the velocity as was shown in the section with the single reflector, and because the geometry of the receivers limits the illuminating angles. We thus obtain a sensitivity energy profile with a single peak. However, the sensitivity energy from the density perturbation does not have such a strong preferred orientation as can be seen in Figure 15 and as was observed above with the single-reflector synthetic model. By selecting six (original) shot gathers based on the density perturbation (at positions -0.341 , -0.085 , 0.0975 , 0.354 , 0.500 , and 0.610 km) that correspond to the maximum sensitivity energy, we again construct images of the baseline and monitor surveys together with their difference (Figure 16d, 16e, and 16f). We observe that we are able to image not only the circle-marked difference observed in Figure 14c but also the region of the reservoir, which was obscured in the difference-image obtained with all data (see regions marked by circles in Figure 16f). This is because we use only the data that contribute to the illumination of the reservoir target zone and therefore increase the S/N of the image for the vicinity of the reservoir region by not including other data that add only noise to that region. For comparison, we also construct images using shot gathers with minimum energy (at positions -1.439 , -1.292 , -0.734 , 0.829 , 1.487 , 1.67 km) (Figure 16g, 16h, and 16i) and with equally distributed position on the surface (at -1.362 , -0.814 , -0.265 , 0.283 , 0.832 , and 1.381 km) (Figure 16j, 16k, and 16l). These results exhibit much poorer resolution of the reservoir region. We conclude that, for imaging the region of interest with a less than ideal acquisition geometry, it is better to estimate the sensitivity from a density perturbation rather than from a velocity perturbation.

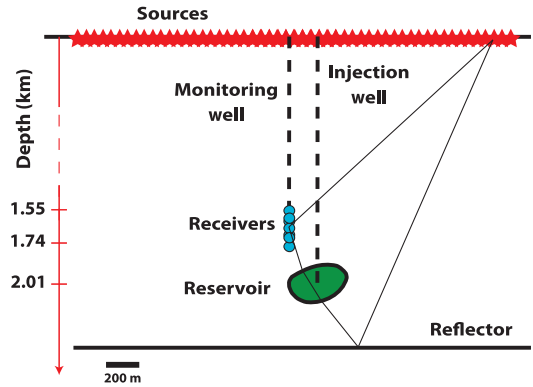


Figure 13. Schematic of the geometry of the SACROC walk-away acquisition.

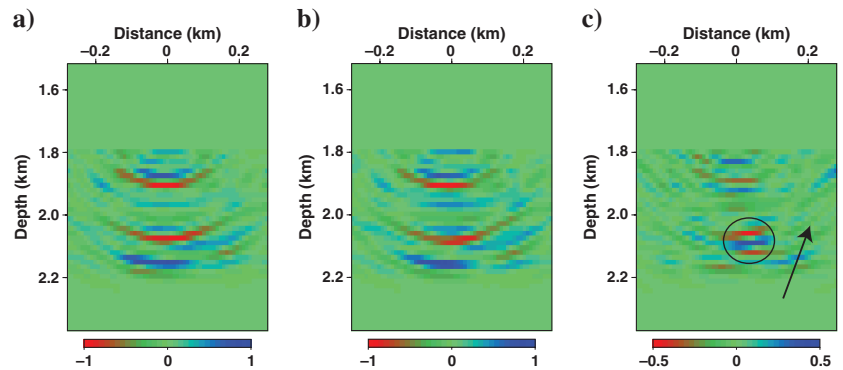


Figure 14. Images obtained using the RTM with all 13 reciprocal shots and 97 reciprocal receivers of: (a) the baseline (2008), (b) the monitor (2009) data sets, and their (c) difference (2008–2009). The region marked with the arrow denotes the location of two injections of CO₂ and the region marked by the circle refers to changes detected from the subtraction of image (a) from image (b). Using the principle of reciprocity, these results are equivalent to images which would be obtained with 97 original shots and 13 original receivers.

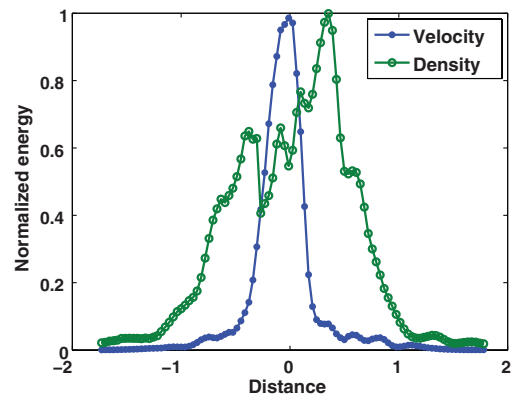


Figure 15. The reverse sensitivity energy profiles indicate the sensitivity of the elliptical perturbation in the velocity and density models to source geometry at the surface. The perturbations in the velocity and density models, positioned at the location of two CO₂ injections, are -1 m/s and -1 kg/m³, respectively, with 50% random noise. The horizontal and vertical diameters of the perturbations are 3 and 2.5 minimum wavelengths, respectively.

DISCUSSION

The examples and results presented in this work illustrate the properties, stability, robustness, and applicability of the RTWS method. Namely, we showed that the RTWS is controlled by four main parameters: the position of the perturbation, the illumination angle (controlled by the position of the source of the input baseline recorded data), the type of perturbation (defining the forward- or backward-scattering), and the scale of the perturbation (depending on the frequency content in the data). There are still many remaining

questions, however. In this section, we will address four of the most pressing.

The first question is how to choose the initial shot gathers with which we estimate the sensitivity. The answer to this question for a walk-away geometry is trivial because all shots have a very similar illumination directionality, and therefore their selection does not significantly affect RTWS. However, for the standard surface seismic acquisition with a general perturbation our observations suggest that for 2D cases, we should start with at least three shots: one from above the perturbation and two others, from either side of

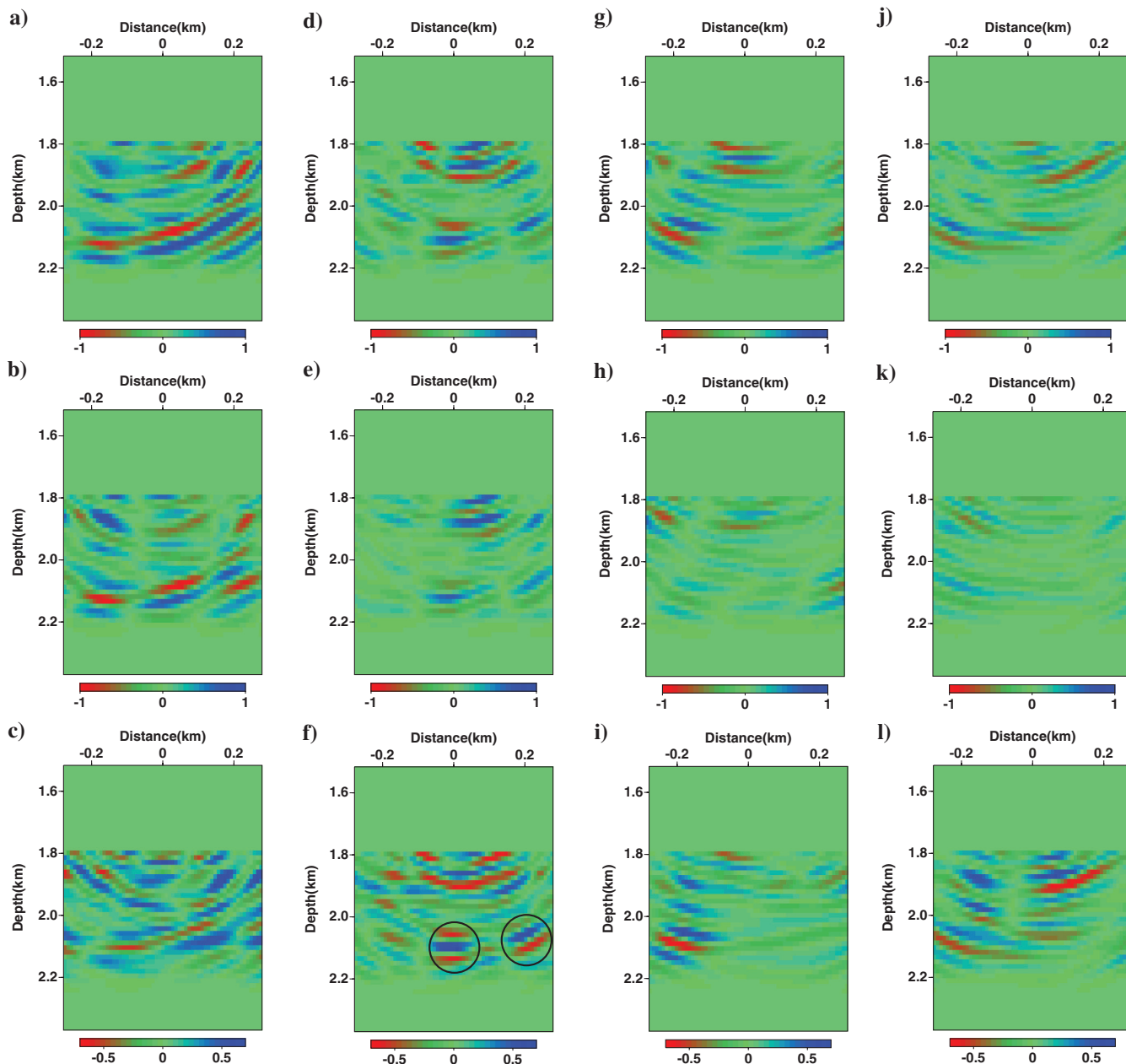


Figure 16. Four sets of RTM images from SACROC, sorted in four columns and three rows, with the data from 2008, 2009, and their difference, respectively, in each column. Each image was migrated with six shots selected based on the maximum sensitivity energy from velocity perturbation (a, b, and c), the maximum sensitivity energy from density perturbation (d, e, and f), the minimum sensitivity energy from density perturbation (g, h, and i), and the equally spaced distances (j, k, and l). The circles in (f) mark the strongest differences between the time-lapse images.

the perturbation, and then add additional equidistant shots from each side. Of course, strategies using information from the previously computed sensitivity profiles could also be used; this is a subject of future research.

The second question is whether we can estimate the sensitivity reliably using baseline data that have limited receiver coverage. In general, RTWS is designed to work with any number of receivers in the data; however, fewer receivers means a less complete back-propagating illuminating wavefield and hence a less complete sensitivity wavefield, and effects like the one seen at the edges of Figure 11a will be more severe.

The third question is what is the minimum number of shots required to image a general perturbation. As shown with the SACROC data, we need to use the geometry of the acquisition and the physics of the scattered-sensitivity wavefield generated by the perturbations. We have shown that the perturbation in the velocity model with general contrast generates stronger forward scattered radiation which can be advantageous for RTWS analysis when we have shots that illuminate the perturbation from multiple directions. In general, to satisfy this criteria we need a wide coverage of sources from different locations at the surface (or in the well). On the other hand, when the acquisition geometry gives poor illumination, the perturbation in density, which results in primarily backward-scattering seems to provide more reliable sensitivity of source locations. In general, we can expect to know whether we are in the single point or the general perturbation sensitivity-scattering regimes: these correspond to an anomaly smaller and larger than one minimum wavelength, respectively. Note that the sources chosen based on RTWS with the density perturbation image the contrasts in density whereas those with the velocity perturbation image the velocity contrasts. The contrasts in the velocity and density models of the target region are assumed to change between time-lapse acquisition.

The fourth question is how we can more accurately estimate the perturbation in the model. The answer to this question lies in the availability of additional information such as injection rates, pressure, temperature, etc., that can give information about a perturbation through the corresponding rock physics model. Methods based on Bayesian inference, for example, could also work to find how the peaks in the energy profiles vary with respect to different types of perturbations. This would require iterations of the RTWS which may become computationally costly, especially when the RTWS analysis is applied in 3D. Note that the general observations and discussions drawn throughout the text in 2D are expected to be similar in 3D.

In general, the computational cost of calculating one shot for RTWS is one and a half times a full finite difference computation. If an RTM algorithm is used to image the subsurface using the baseline data set, then RTWS can be incorporated into RTM and only the sensitivity-scattered wavefield will require additional computation. This is roughly half of an entire propagation. Our analysis requires a relatively small number of shots, however, making this computational cost negligible in comparison with the collection of the entire monitor data set, and more importantly improves our ability to image the region of interest.

CONCLUSIONS

In this study, we presented a data-driven method, RTWS, for estimating the sensitivity of the changes of a predefined region of interest to source geometry. We tested this method with three

examples: two synthetic models, and one real time-lapse data set from the SACROC field. Our synthetic examples illustrate the advantages of the RTWS method over the forward sensitivity approach; in particular, they demonstrate the robustness of RTWS to errors in the background velocity model. The synthetic examples also illustrate the stability of the RTWS method to noise in the model, to errors in the a priori estimated perturbation, and to different input data. The field data example shows how using the RTWS method we can image a region of interest within a reservoir with higher S/N by using only the most sensitive shots. In addition, the synthetic examples show that a reliable estimate of the sensitivity energy profile for source geometry can be made with relatively few back-propagated shot gathers, making the RTWS method attractive and efficient for reducing the cost of time-lapse target-oriented acquisition and imaging.

ACKNOWLEDGMENTS

We thank Total S. A. and the founding members of the Earth Resources Laboratory at MIT for funding this work. We acknowledge Yingcai Zheng for insightful discussions, Lianjie Huang for providing the data, and Di Yang for providing the initial models from the SACROC field. We are also grateful to Clement Kostov and two anonymous reviewers, whose comments helped significantly to improve the manuscript.

APPENDIX A

REVERSE-TIME ACOUSTIC WAVE SENSITIVITY

The derivation of the reverse-time wave sensitivity can be derived similarly as in Denli and Huang (2010) by taking a derivative either with respect to velocity or density. However, to estimate the sensitivity of both parameters simultaneously, we need to derive these equations using perturbation analysis. For the sake of simplicity, we use the acoustic wave equation with varying velocity and density

$$\rho \nabla \cdot \frac{1}{\rho} \nabla P - \frac{1}{c^2} \frac{\partial^2 P}{\partial t^2} - f = 0, \quad (\text{A-1})$$

where $c(\mathbf{x})$ is wave velocity (speed), $\rho(\mathbf{x})$ is density, and $P(\mathbf{x}, t)$ and $f(\mathbf{x}, t)$ are pressure field and source function, respectively.

Suppose we have two pressure fields which solve equation A-1 with the same source f but with different acoustic velocities c_j and densities ρ_j ,

$$\rho_j \nabla \cdot \frac{1}{\rho_j} \nabla P_j - \frac{1}{c_j^2} \frac{\partial^2 P_j}{\partial t^2} - f = 0, \quad (\text{A-2})$$

where $j = 1, 2$ refer to a baseline and monitor, respectively.

By taking the difference of these two equations, we obtain

$$\begin{aligned} \rho_2 \nabla \cdot \frac{1}{\rho_2} \nabla P_2 - \frac{1}{c_2^2} \frac{\partial^2 P_2}{\partial t^2} - f - \rho_1 \nabla \cdot \frac{1}{\rho_1} \nabla P_1 \\ + \frac{1}{c_1^2} \frac{\partial^2 P_1}{\partial t^2} + f = 0. \end{aligned} \quad (\text{A-3})$$

Using the first order approximation for acoustic velocity and density,

$$\frac{1}{\rho_2(\mathbf{x})} = \frac{1}{\rho_1(\mathbf{x})} - \frac{\delta\rho(\mathbf{x})}{\rho_1^2(\mathbf{x})} \quad (\text{A-4})$$

and

$$\frac{1}{c_2^2(\mathbf{x})} = \frac{1}{c_1^2(\mathbf{x})} - \frac{2\delta c(\mathbf{x})}{c_1^3(\mathbf{x})}, \quad (\text{A-5})$$

we obtain

$$\begin{aligned} \rho_2 \nabla \cdot \frac{1}{\rho_2} \nabla P_2 - \frac{1}{c_2^2} \frac{\partial^2 P_2}{\partial t^2} - (\rho_2 - \delta\rho) \nabla \cdot \left(\frac{1}{\rho_2} + \frac{\delta\rho}{\rho_1^2} \right) \nabla P_1 \\ + \left(\frac{1}{c_2^2} + \frac{2\delta c}{c_1^3} \right) \frac{\partial^2 P_1}{\partial t^2} = 0. \end{aligned} \quad (\text{A-6})$$

Expanding and neglecting higher-order terms gives

$$\begin{aligned} \rho_2 \nabla \cdot \frac{1}{\rho_2} \nabla (P_2 - P_1) - \frac{1}{c_2^2} \frac{\partial^2 (P_2 - P_1)}{\partial t^2} - \rho_2 \nabla \cdot \frac{\delta\rho}{\rho_1^2} \nabla P_1 \\ + \delta\rho \nabla \cdot \frac{1}{\rho_2} \nabla P_1 + \frac{2\delta c}{c_1^3} \frac{\partial^2 P_1}{\partial t^2} = 0. \end{aligned} \quad (\text{A-7})$$

By defining sensitivity field S as

$$S = P_2 - P_1, \quad (\text{A-8})$$

and the perturbation source \hat{f}

$$\hat{f} = VP_1, \quad (\text{A-9})$$

where $V(\mathbf{x}, t)$ is a perturbation operator which defined as,

$$V = \rho_2 \nabla \cdot \frac{\delta\rho}{\rho_1^2} \nabla - \delta\rho \nabla \cdot \frac{1}{\rho_2} \nabla - \frac{2\delta c}{c_1^3} \frac{\partial^2}{\partial t^2}. \quad (\text{A-10})$$

Equation A-7 becomes

$$\rho_2 \nabla \cdot \frac{1}{\rho_2} \nabla S - \frac{1}{c_2^2} \frac{\partial^2 S}{\partial t^2} - \hat{f} = 0. \quad (\text{A-11})$$

To find S with this method, we concurrently solve equation A-2 with $j = 1$ to find P_1 and equation A-11 to find S using equation A-9 to compute \hat{f} .

For the sake of consistency, we replace the baseline wavefield P_1 by P and the subscripts of the baseline and monitor velocity and

density models $j = 1, 2$ by b, p , respectively. Then, this algorithm can be summarized by the system given in equation 1.

REFERENCES

- Aki, K., and P. G. Richards, 1980, Quantitative seismology, theory and methods, **2**.
- Baysal, E., D. Kosloff, and W. C. Sherwood, 1983, Reverse time migration: *Geophysics*, **48**, 1514–1524, doi: [10.1190/1.1441434](https://doi.org/10.1190/1.1441434).
- Bear, G., C.-P. Lu, R. Lu, D. Willen, and I. Watson, 2000, The construction of subsurface illumination and amplitude maps via ray tracing: *The Leading Edge*, **19**, 726–728, doi: [10.1190/1.1438700](https://doi.org/10.1190/1.1438700).
- Carcione, J., 1999, Staggered mesh for the anisotropic and viscoelastic wave equation: *Geophysics*, **64**, 1863–1866, doi: [10.1190/1.1444692](https://doi.org/10.1190/1.1444692).
- Cheng, A., L. Huang, and J. Rutledge, 2010, Time-lapse VSP data processing for monitoring CO₂ injection: *The Leading Edge*, **29**, 196–199, doi: [10.1190/1.3304824](https://doi.org/10.1190/1.3304824).
- Curtis, A., 1999, Optimal design of focused experiments and surveys: *Geophysical Journal International*, **139**, 205–215, doi: [10.1046/j.1365-246X.1999.00947.x](https://doi.org/10.1046/j.1365-246X.1999.00947.x).
- Denli, H., and L. Huang, 2010, Elastic wave sensitivity propagation: *Geophysics*, **75**, no. 3, T83–T97, doi: [10.1190/1.3428403](https://doi.org/10.1190/1.3428403).
- Hoffmann, J., 2001, Illumination, resolution, and image quality of PP- and PS- waves for survey planning: *The Leading Edge*, **20**, 1008–1014, doi: [10.1190/1.1487305](https://doi.org/10.1190/1.1487305).
- Khodja, M., M. Prange, and H. Djikpesse, 2010, Guided Bayesian optimal experimental design: *Inverse Problems*, **26**, IOP Publishing.
- Kosloff, D., and E. Baysal, 1982, Forward modeling by a Fourier method: *Geophysics*, **47**, 1402–1412, doi: [10.1190/1.1441288](https://doi.org/10.1190/1.1441288).
- Marcinkovich, C., and K. Olsen, 2003, On the implementation of perfectly matched layers in a three-dimensional fourth-order velocity-stress finite difference scheme: *Journal of Geophysical Research*, **108**, 18:1–16, doi: [10.1029/2002JB002235](https://doi.org/10.1029/2002JB002235).
- van den Berg, J., and A. Curtis, 2003, Optimal nonlinear Bayesian experimental design: An application to amplitude versus offset experiments: *Geophysical Journal International*, **155**, 411–421, doi: [10.1046/j.1365-246X.2003.02048.x](https://doi.org/10.1046/j.1365-246X.2003.02048.x).
- Versteeg, R., and G. Grau, 1991, The Marmousi experience: 52nd Annual International Conference and Exhibition, EAGE, Extended Abstracts.
- Wang, Y., L. Huang, and Z. Zhang, 2011, Reverse-time migration of time-lapse walkaway VSP data for monitoring CO₂ injection at the SACROC EOR field: 81st Annual International Meeting, SEG, Expanded Abstracts, 4304–4308.
- Wu, R.-S., 1989, The perturbation method in elastic wave scattering: *Pure and Applied Geophysics*, **131**, 605–637, doi: [10.1007/BF00876266](https://doi.org/10.1007/BF00876266).
- Xie, X.-B., S. Jin, and R.-S. Wu, 2006, Wave-equation-based seismic illumination analysis: *Geophysics*, **71**, no. 5, S169–S177, doi: [10.1190/1.2227619](https://doi.org/10.1190/1.2227619).
- Xie, X.-B., and H. Yang, 2008, A full-wave equation based seismic illumination analysis method: 70th Annual International Conference and Exhibition, EAGE, Extended Abstracts, P284.
- Yang, D., M. Fehler, A. Malcolm, and L. Huang, 2011, Carbon sequestration monitoring with acoustic double-difference waveform inversion: A case study on SACROC walkaway VSP data: 81st Annual International Meeting, SEG, Expanded Abstracts, 4273–4277.
- Youn, O., and H.-W. Zhou, 2001, Depth imaging with multiples: *Geophysics*, **66**, 246–255, doi: [10.1190/1.1444901](https://doi.org/10.1190/1.1444901).